10.2514/6.2016-1708
AIAA SciTech Forum
4-8 January 2016, San Diego, California, USA
57th AIAA/ASCE/AHS/ASC Structures, Structural Dynamics, and Materials Conference

Large Deformation Modeling of a Beam Type Structure and a 3D Wingbox using an Enhanced Modal Approach

Markus Ritter*
DLR - Institute of Aeroelasticity, Bunsenstraße 10, 37073 Göttingen, Germany
Carlos E.S. Cesnik †
University of Michigan, Ann Arbor, Michigan 48109-2140

A recently developed modal-based method that captures the geometric nonlinear effects that arise in the regime of large deformations of wing-like structures is applied to the modeling of a highly flexible beam structure and a 3D wingbox configuration. The method features quadratic and cubic stiffness terms and calculates the nodal deformation field not only by normal modes but also by additional mode components up to fourth order. Thus, both a nonlinear force-displacement relationship and a geometrically nonlinear displacement field are accounted for. Static and dynamic results for the two configurations are presented together with results from a commercial finite element solver and from the *UM/NAST* aeroelastic solver from the University of Michigan. The numerical study highlights the capability of the method to capture the nonlinear effects and demonstrates its power to model a 3D wingbox structure made of shell elements with anisotropic material characteristics.

I. Introduction

THERE is a significant interest in the development of future passenger transport aircraft with lower emissions and higher fuel efficiency. One of the key design features that supports achieving such goals is longer span wings, where induced drag is reduced. As the span increases along with the wing's aspect ratio, it leads to higher flexibility. This geometric effect becomes inevitable as light, high performance structural construction is used. An increased structural flexibility is advantageous when dealing with external disturbances, such as gust encounters, due to the reduced rigid body acceleration. However, it brings several challenges related to the modeling, analysis, and design and it becomes inevitable that the geometrically nonlinear structural nature of the vehicle be taken into account in the earliest phases of design.[1]

Industry-standard aeroelastic simulation frameworks are typically based on a modal description of the airframe where eigenvectors and corresponding eigenvalues in the frequency range of interest are used to calculate structural deformations in a linear way. These have limited if any applicability for the problem of geometrically nonlinear aeroelasticity, where the emphasis turns to time-domain solutions and coupled aeroelasticity/flight dynamics analysis (due to the coupled nature of the rigid body and elastic response of the aircraft). Geometrically-exact beam-based formulations coupled with appropriate unsteady aerodynamics make the state of the art in solution frameworks for this type of problem.[2] On the other hand, beam formulations may not be sufficient to model complex structural details of transport aircraft wings and the use of nonlinear FE codes for aeroelastic simulations can become very costly, especially for dynamic simulations.

A recently developed method (refered to as *Enhanced Modal Approach*) extends the classical modal approach towards large deformations.[3] This method uses a higher order strain energy formulation to consider nonlinear force-displacement relationships and higher-order mode components for the reconstruction of a

*Research Engineer, AIAA Member (markus.ritter@dlr.de)
†Professor, Department of Aerospace Engineering, Fellow, AIAA (cesnik@umich.edu)

geometrically nonlinear displacement field. Both enhancements are derived by Taylor series expansions; a series of static, nonlinear structural simulations of the structure considered is necessary to identify the higher-order components. Once these components are determined, static and dynamic simulations with the method can be done with a computational effort which is only slightly increased compared to the classical modal approach.

The ability to model complex, highly flexible 3D FEM structures statically and dynamically is seen as the ultimate goal of the enhanced modal approach. A model of this type is shown in Fig. 1 as a motivating example. A step by step approach must be followed to achieve this goal. Thus the method proposed is applied to different structural test cases with increasing complexity to identify possible issues and improve the method gradually.

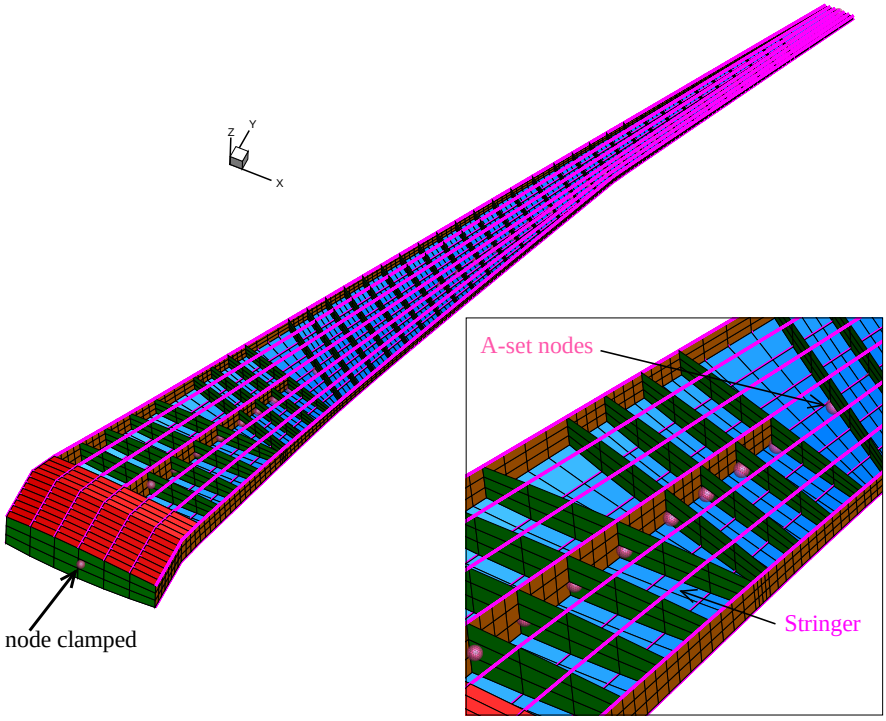

Figure 1. 3D FEM model of a transport aircraft wing built with spars, ribs, stringers, and skins as a motivating test case for future application of the method proposed.

This work presents applications of the method to a beam type structure and a more complex, slender 3D wingbox modeled by shell elements made from fiber reinforced material with anisotropic characteristics.

Methods for the reduced order modeling (ROM) of nonlinear structures have been adressed by several authors. Mignolet and co-workers have given detailed descriptions for the derivation of static and dynamic nonlinear structural governing equations including quadratic and cubic stiffness coefficients. The field of application ranges from plate structures to curved beams and the modeling of a complex UAV wing.[4,5,6]

Kuether and Allen describe methods based on nonlinear normal modes (NNMs) to simplify large, complex structures. NNMs basically describe the resonant frequency and response of a structure as a function of response amplitude or energy.[7,8] Two substructuring methods that can be used in conjunction with detailed finite element models are presented by Kuether,[7] where the second one is based on creating a reduced order model of a structure by applying a series of static loads to a nonlinear FE model. Quadratic and cubic stiffness terms are used to consider nonlinear force displacement behaviour and coupling of individual modes.

As will be shown, the kinematically nonlinear displacement field present in large deformations of wing-like structures can be reconstructed by shape functions of higher order. The method of quadratic components was successfully applied by Segalman and Dohrmann to improve the kinematical and dynamical description of rotating structures (beams) undergoing large displacements.[9,10] This method is also used by van Zyl for the calculation of T-Tail flutter.[11,12] In the approach presented, the concept of higher-order modes is further

developed to better reconstruct nonlinear, large displacements. Higher-order stiffness coefficients derived here from a higher-order strain energy formulation are used to represent a nonlinear force-displacement behaviour.

II. Derivation of the Enhanced Modal Approach

The derivation of the enhanced modal approach is given in detail in Ref.[3] and recapitulated in a more compact form in the following.

Compared to the classical modal approach, the proposed method is based upon considering a nonlinear force-displacement relationship by quadratic and cubic stiffness terms and a geometrically nonlinear displacement field based on higher-order mode components up to fourth order. Furthermore, the generalized forces are dependent on the state of deformation and the nodal force field applied.

II.A. Static formulation: Higher-order strain energy

The total potential energy of an elastic body U consists of the sum of the total strain energy U and the potential energy of the applied loads V. This statement is expressed as:[13]

$$\pi = U + V \ . \tag{1}$$

Assuming linear elastic material behaviour (Hooke's law), and neglecting the influence of temperature, the total strain energy U in the body is given as (here and what follows, the Einstein notation is used):

$$U = \frac{1}{2} \int_V \tau_{ij} \epsilon_{ij} \, dv \ \ (i,j = 1,2,3) \ , \tag{2}$$

where τ_{ij} and ϵ_{ij} are the stress and strain component pairs, respectively. The work done by the applied loads V can be expressed as:

$$V = \int_V B_i \, u_i \, dv + \int_S T_i^{(\nu)} u_i \, ds \ , \tag{3}$$

where B_i represents the components of the applied body forces, u_i the components of the displacement field, and $T_i^{(\nu)}$ denotes the traction vector applied on the body surface.

Introducing a variation of both the total strain energy and the external work yields:

$$\delta\pi = \delta(U+V) = \int_V \tau_{ij} \, \delta\epsilon_{ij} \, dv - \int_V B_i \, \delta u_i \, dv - \int_S T_i^{(\nu)} \delta u_i \, ds \ . \tag{4}$$

Invoking the Principle of Minimum Total Potential Energy, i.e., $\delta\pi = 0$, yields the variation of the total strain energy equals the negative variation of the external work:

$$\delta U = -\delta V \ . \tag{5}$$

Now the total strain energy, Eq.(2), is assumed to be a *nonlinear* and continuously differentiable function of a scalar value q_i of a number of generalized cordinates, m, and expanded in a Taylor series up to the fourth order centered at zero (since the internal energy is zero for zero deformation):

$$\begin{aligned} U(\boldsymbol{q}) = & \frac{1}{2!} \sum_{i=1}^{m} \sum_{j=1}^{m} \frac{\partial^2 U}{\partial q_i \, \partial q_j} \, q_i \, q_j \\ & + \frac{1}{3!} \sum_{i=1}^{m} \sum_{j=1}^{m} \sum_{k=1}^{m} \frac{\partial^3 U}{\partial q_i \, \partial q_j \, \partial q_k} \, q_i \, q_j \, q_k \\ & + \frac{1}{4!} \sum_{i=1}^{m} \sum_{j=1}^{m} \sum_{k=1}^{m} \sum_{l=1}^{m} \frac{\partial^4 U}{\partial q_i \, \partial q_j \, \partial q_k \, \partial q_l} \, q_i \, q_j \, q_k \, q_l \ + h.o.t. \end{aligned} \tag{6}$$

Using Castigliano's first theorem and applying a differentiation with respect to $\boldsymbol{q}$ centered at zero yields a governing equation of the structure as a function of $\boldsymbol{q}$.[13] This governing equation comprises quadratic and cubic stiffness dependencies and thus accounts for a nonlinear force-deformation behaviour:

$$\begin{aligned}\frac{\partial U}{\partial q_p} &= \sum_{i=1}^{m} \frac{\partial^2 U}{\partial q_i\, \partial q_p}\, q_i \\ &+ \frac{1}{2!} \sum_{i=1}^{m}\sum_{j=1}^{m} \frac{\partial^3 U}{\partial q_i\, \partial q_j\, \partial q_p}\, q_i\, q_j \\ &+ \frac{1}{3!} \sum_{i=1}^{m}\sum_{j=1}^{m}\sum_{k=1}^{m} \frac{\partial^4 U}{\partial q_i\, \partial q_j\, \partial q_k\, \partial q_p}\, q_i\, q_j\, q_k \; + h.o.t. \end{aligned} \tag{7}$$

Introducing the definitions ${}^pG_n$ for the partial derivatives in Eq.(7), the following equation in the pseudo-generalized coordinates is obtained and used as the basis for the method:

$${}^pG_1^i\, q_i \; + \; {}^pG_2^{ij}\, q_i q_j \; + \; {}^pG_3^{ijk}\, q_i q_j q_k = Q^p \;\; (p = 1, \ldots, m) \tag{8}$$

Here the summation convention is used again. The idea of the proposed method is to take the ${}^pG_n$ stiffness matrices as generalized stiffnesses and the $\boldsymbol{q}$ as generalized coordinates. The stiffness parameters G_n can be determined by polynomial fitting or numerical differentiation.[3]

II.B. Static formulation: Higher-order deformation reconstruction

The second extension is the reconstruction of the geometrically nonlinear displacement field. As mentioned above, the nonlinear static FE analysis excites nonlinear terms in the strain energy, but also a nonlinear displacement field.

In this work, the nodal deformation field is expanded in a Taylor series centered at zero (similar to the strain energy) which is truncated after the fourth term:

$$\mathbf{u}(\boldsymbol{q}) = \sum_{i=1}^{m} \frac{\partial \mathbf{u}}{\partial q_i}\, q_i \tag{9}$$

$$+ \frac{1}{2!} \sum_{i=1}^{m}\sum_{j=1}^{m} \frac{\partial^2 \mathbf{u}}{\partial q_i \partial q_j}\, q_i\, q_j \tag{10}$$

$$+ \frac{1}{3!} \sum_{i=1}^{m}\sum_{j=1}^{m}\sum_{k=1}^{m} \frac{\partial^3 \mathbf{u}}{\partial q_i \partial q_j \partial q_k}\, q_i\, q_j\, q_k \tag{11}$$

$$+ \frac{1}{4!} \sum_{i=1}^{m}\sum_{j=1}^{m}\sum_{k=1}^{m}\sum_{l=1}^{m} \frac{\partial^4 \mathbf{u}}{\partial q_i \partial q_j \partial q_k \partial q_l}\, q_i\, q_j\, q_k q_l \; + h.o.t. \tag{12}$$

Partial differentiation of the displacement field defined in this way with respect to the generalized coordinates and substitution similar as above for the strain energy yields:

$${}^p\boldsymbol{\Phi} = \frac{\partial \mathbf{u}}{\partial q_p} = {}^p\boldsymbol{\Phi}_0 + {}^p\boldsymbol{\Phi}_1^i\, q_i + {}^p\boldsymbol{\Phi}_2^{ij}\, q_i q_j + {}^p\boldsymbol{\Phi}_3^{ijk}\, q_i q_j q_k \tag{13}$$

The term ${}^p\boldsymbol{\Phi}_0$ can be seen as the equivalent of the structure's normal modes.

II.B.1. The generalized forces and the final governing equation

Considering Eq.(8), the forcing term of the structure's governing equation consists of the generalized force Q^p. Applying the principle of virtual work and the Taylor series expansion of the higher order mode components results in an extension of the generalized forces. For simplicity, the approach described by van Zyl is followed here and only the linear and the quadratic mode shape components are considered for the virtual work:[12]

$$\delta V = \delta \mathbf{u}^T \boldsymbol{f} \;\; , \tag{14}$$

where $\boldsymbol{f}$ denotes an arbitrary nodal force field. Expansion of the virtual physical displacements $\delta\mathbf{u}$ using the linear and the quadratic mode shapes yields:

$$\delta V = \delta q_p^T \left({}^p\boldsymbol{\Phi}_0{}^T + {}^p\boldsymbol{\Phi}_1^i{}^T q_i \right) \boldsymbol{f} \ . \tag{15}$$

Thus the generalized forces are given as:

$$Q^p = {}^p\boldsymbol{\Phi}_0{}^T \boldsymbol{f} + {}^p\boldsymbol{\Phi}_1^i{}^T \boldsymbol{f}\, q_i \ . \tag{16}$$

Combining Eq.(8) and (16) yields:

$$({}^pG_1^i - {}^p\boldsymbol{\Phi}_1^i{}^T \boldsymbol{f}\,)\, q_i + {}^pG_2^{ij}\, q_i\, q_j + {}^pG_3^{ijk}\, q_i\, q_j\, q_k = {}^p\boldsymbol{\Phi}_0{}^T \boldsymbol{f} \ . \tag{17}$$

Eq.(17) is the static governing equation of the enhanced modal approach. Compared to the classical modal approach, it can be seen that the ${}^pG_1^i$ term is amended by the product of the transpose of the quadratic mode component matrix and the force field. This additional stiffness parameter is proportional to the force field applied to the structure and induces a coupling of the otherwise (in the linear sense) uncoupled eigenvectors.

Following the solution of Eq.(17), the nodal deformation field is reconstructed as function of the generalized coordinates $\boldsymbol{q}$:

$$\mathbf{u}(\boldsymbol{q}) = {}^p\boldsymbol{\Phi}_0\, q_p + {}^p\boldsymbol{\Phi}_1^i\, q_p q_i + {}^p\boldsymbol{\Phi}_2^{ij}\, q_p q_i q_j + {}^p\boldsymbol{\Phi}_3^{ijk}\, q_p q_i q_j q_k \ , \tag{18}$$

where the sum is taken again over repeated indices.

II.C. Dynamic formulation

The dynamic formulation is obtained by adding inertia terms to Eq.(17). The governing equation is then given as (neglecting velocity-dependent damping forces for simplicity):

$$\boldsymbol{M}\ddot{q}_i + \left({}^pG_1^i - {}^p\boldsymbol{\Phi}_1^i{}^T \boldsymbol{f} \right) q_i + {}^pG_2^{ij}\, q_i\, q_j + {}^pG_3^{ijk}\, q_i\, q_j\, q_k = {}^p\boldsymbol{\Phi}_0{}^T \boldsymbol{f} \ , \tag{19}$$

with $\boldsymbol{M}$ denoting the generalized mass matrix.

III. Numerical Studies

The results of selected static and dynamic simulations obtained with the method described are presented in the following sections. Furthermore, the test case presented here was modeled with University of Michigan's UM/NAST solver. This toolbox provides excellent reference data in terms of nonlinear structural dynamics and coupled aeroelastic simulations.[14]

III.A. Cantilever Beam Test Case

The first test case consists of a highly flexible beam model with a length of 16 meters. It is discretized by 32 beam finite elements and 33 nodes. The moments of inertia vary quadratically along the beam axis to obtain bending deformations with constant curvature. The layout of the model is shown in Fig. 2. Displacement of node 33 (outermost node) is used to show the behaviour of the beam and the method for dynamic loadings. For all simulations with the proposed method, only seven selected mode shapes were used. Thus the higher

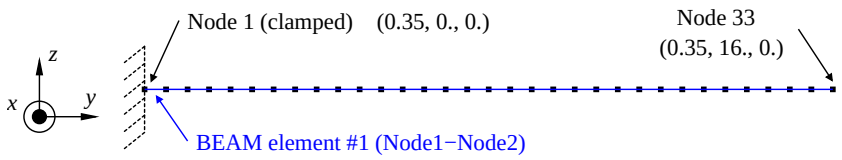

Figure 2. 16m beam FE model, 33 Nodes, clamping at Node 1

order stiffness matrices and mode components (G and $\boldsymbol{\Phi}$, respectively) were calculated for these modes. The

selected modes were found to be sufficient to obtain convergence in terms of the static deformation field; also the computational effort is reduced when considering less modes especially for the dynamic simulations. The values of ${}^{p}G_1^i$ and ${}^{p}\mathbf{\Phi}_1^i$ reconstructed with the method summarized here and described in Ref. 3 are very close to the corresponding values from the natural eigenvalues of the beam. Table 1 lists the types and frequencies of the 10 lowest mode shapes of the beam model obtained from the finite element modal analysis. Additionally, the eigenvalues from the reconstruction method are given for the seven selected modes. The second, third, and fourth in-plane bending mode were omitted.

Table 1. Eigenvalues of the ten lowest modes of the beam model; values were obtained from a FE analysis and from a polynomial reconstruction method.

Mode	Type of mode	Eigenvalue FE analysis [Hz]	Eigenvalue reconstructed [Hz]
1	first bending	0.595	0.595
2	first bending in-plane	1.190	1.190
3	second bending	2.705	2.705
4	second bending in-plane	5.407	-
5	third bending	6.956	6.956
6	fourth bending	13.358	13.358
7	third bending in-plane	13.893	-
8	fifth bending	21.908	21.908
9	fourth bending in-plane	26.651	-
10	first torsion	27.132	27.132

III.B. Static simulations and validation of the beam test case with nonlinear data from UM/NAST

A constant tip force in the z direction was applied at the outermost node of the beam with assumed values between 500 N and 3000 N to simulate a constant static loading. The results of this test case are presented in Fig. 3. No follower forces and no gravity have been considered in the static solutions. In a full nonlinear solution sequence (considering incremental loads), the force applied to the beam is increased stepwise and equilibrium is ensured in every step until the specified load is applied. In the solution sequence used for the enhanced modal approach, the specified value of the force is applied always onto the undeformed initial configuration of the beam. The values were chosen to excite deformations of the beam beyond the limit of structural linearity. This can be seen in terms of the displacement of the beam in z and in y directions. The linear FE solution yields too large displacements in the z direction and of course omits the displacement in the y direction completely. The results of the new method are in good agreement with the nonlinear reference data from UM/NAST, and the displacement in the z and in the y directions are captured well up to the tip force of 2500 N. Differences between the enhanced modal approach and the nonlinear reference data become larger starting at the tip force of 3000 N. For this force, the bending deformation in the z direction reaches a value of 25% of the span of the beam. An interesting point is that the nonlinear deformation fields are "on top" of the linear one but with the foreshortening effect keeping the beam length constant.

III.C. Dynamic simulations and validation of the beam test case with nonlinear data from UM/NAST

The dynamic validation of the method was done applying a harmonically oscillating force onto the outermost node of the beam. Again, no structural damping, no follower forces, and no gravity were considered. The initial conditions for the generalized displacements and the generalized velocities were set to zero. The results are shown in Fig. 4. Despite a good overall agreement between the UM/NAST results and the results of the proposed method, differences occur both for the deformation in the z and in the y direction. It must be mentioned that the results of the proposed method were calculated including only five bending modes.

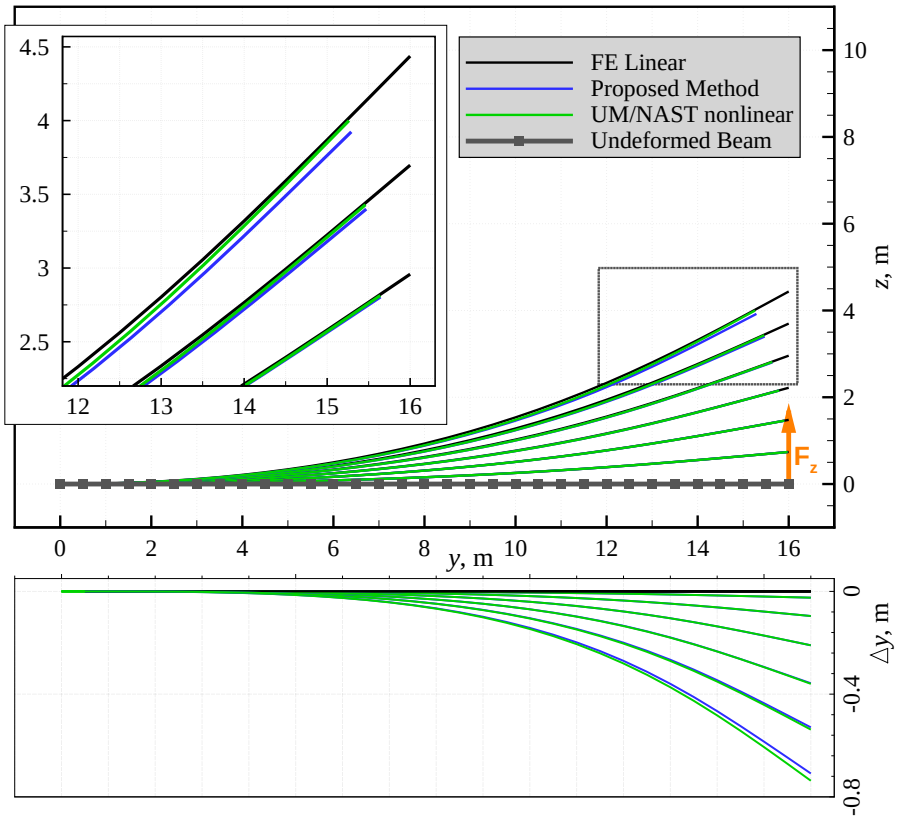

Figure 3. Comparison of the static displacement fields obtained by different methods for forces with values of 500, 1000, 1500, 2000, 2500, and 3000 N applied along the z direction at the end of the beam.

III.D. Static and dynamic aeroelastic simulations and validation with UM/NAST results

For the enhanced modal approach, a vortex-lattice solver was used that provides the aerodynamic forces. The solver is part of the in-house aeroelastic toolbox *Eques* and implemented such that the aerodynamic panels can undergo any kind of translation and rotation due to elastic deformations. The force transfer from the aerodynamic panels onto the structural grid is done via the transposed of a coupling matrix.[15] Transforming aerodynamic forces into equivalent forces on the beam's nodes requires the calculation of forces and moments. In this case, another approach was used to avoid the calculation of moments. A so-called coupling model was built which uses rigid-bar elements that are connected to a beam node at one side each. The other end of the rigid-bar elements are used as coupling points to where the aerodynamic forces are transferred.

The coupling approach described and part of the vortex-lattice grid are depicted in Fig. 5. To obtain deformations of the coupled aeroelastic system ranging from the linear to the nonlinear regime, the root angle of attack (AoA) was varied within the range of one to five degrees in steps of one degree. UM/NAST uses a strip-theory aerodynamic model. However, UM/NAST enables the correction of the static force produced by each strip by considering a weighting factor that accounts for wingtip effects. The correction factors for UM/NAST were taken from the lift distribution given by the vortex-lattice solver for the rigid wing. This correction method results in identical aerodynamic forces for the vortex-lattice and the UM/NAST aerodynamic solvers for the undeformed wing.

Results of the static coupling simulations are shown in Fig. 6 in terms of the bending deformations of the beam. For this test case, results from Nastran SOL144 solution sequence (static aeroelastic) are also presented. The level of difficulty is increased for these simulations compared to the static simulations with a constant force in the z direction, since the forces on the nodes now have contributions along the y direction as well. The bending deformation from the proposed method agrees well with the results from UM/NAST. At higher angles of attack, the difference between the linear and the nonlinear solutions becomes larger and the beam tends to have a reduced deformation in the UM/NAST results. This can be seen as realistic, since the

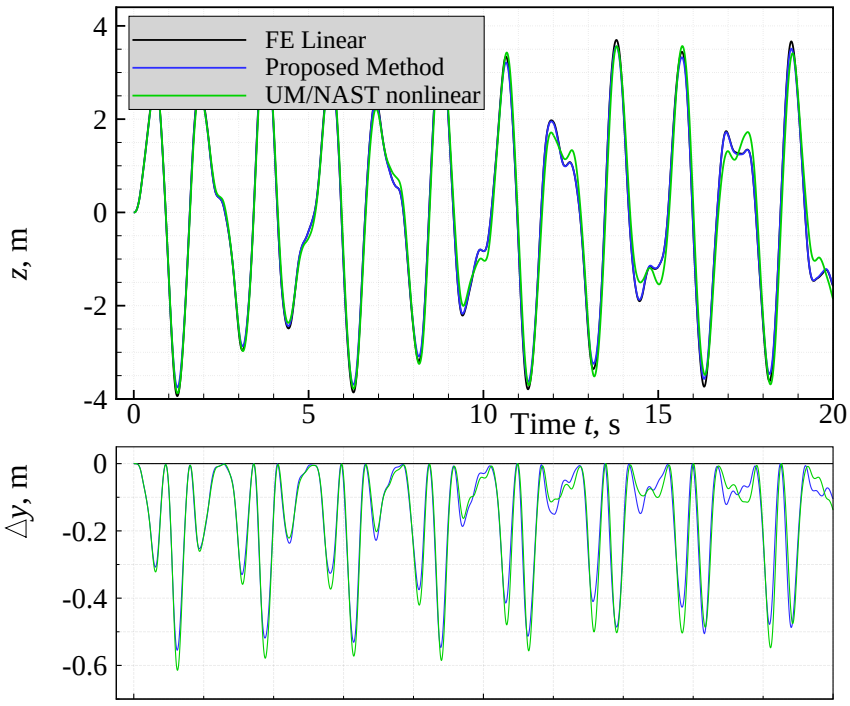

Figure 4. Comparison of the unsteady displacement field obtained by different methods for a sinusoidal tip force applied at the end of the beam. Force amplitude = 2000 N, frequency = 1.0 Hz.

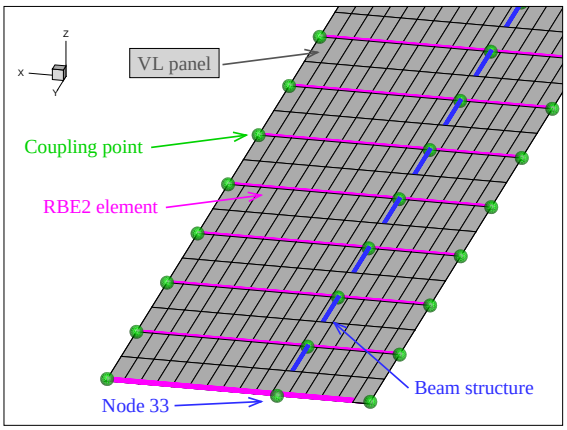

Figure 5. Depiction of the coupling approach: Aerodynamic forces are transformed onto the structure's coupling points and then transferred implicitly to the beam's nodes via rigid-bar elements.

forces are always applied onto the undeformed structure (in the linear and the enhanced modal approach), but the enhanced modal approach considers the "in-plane" force due to the quadratic mode component.

The unsteady version of the VL solver, named UVL in the following, uses a wake-stepping method to account for the unsteady circulation on body and wake panels.[16] An implicit BDF scheme is applied to march the solution forward in time. The timestepsize for all unsteady simulations was set to 0.001s, which was found to be sufficiently small for a good resolution of the gust in terms of aerodynamic forces. Unsteady reference solutions were obtained by Nastran's SOL146 sequence. This frequency domain method allows the specification of gusts with prescribed disturbance velocities in the z direction and corresponding gust gradients. An inverse Fourier transformation is applied to the frequency domain results within Nastran to obtain time domain results in terms of displacements of selected structural nodes. Results of the dynamic coupled simulations are presented in Fig. 7 as function of time for the z, the y, and the x displacements at the end of the beam. The gust disturbance velocity in the z direction, U_g, and the gust gradient, H_g,

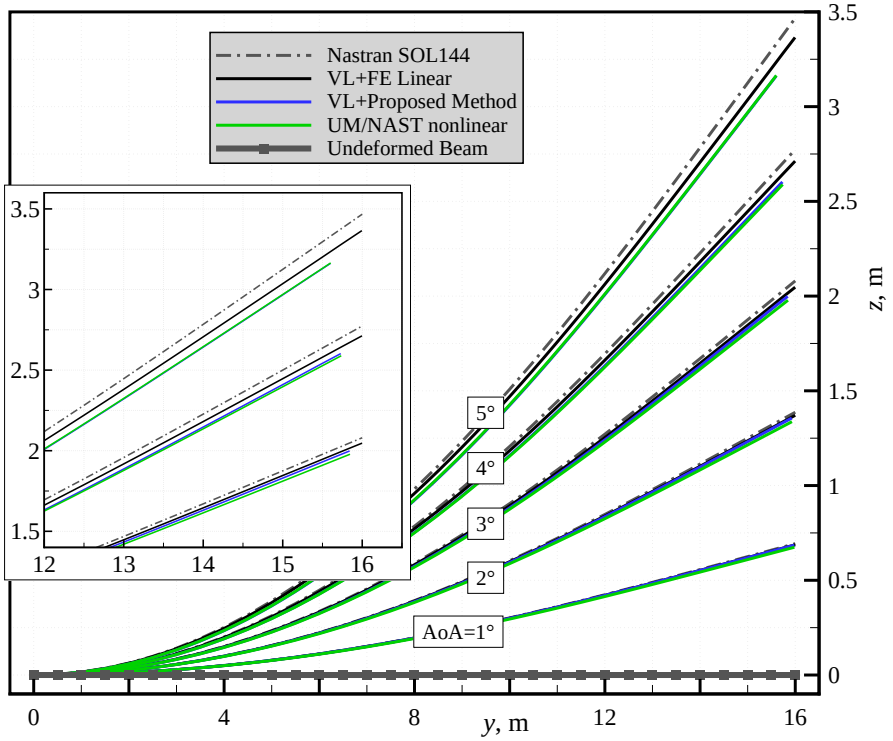

Figure 6. Comparison of static coupling results calculated by different methods.

were chosen to excite deformations in the nonlinear regime. Here, U_g was set to $20\,m/s$ and H_g to $5\,m$, which yields a maximum displacement of about 22% of the span of the wing. From an aerodynamic point of view, this gust disturbance velocity is extremely large, but no stall effects were taken into account to obtain high unsteady aerodynamic forces for high structural excitation. Larger differences are obtained between the three solution methods. The proposed method yields less displacement in the z and in the y directions at the wing tip. Both the displacement in the y and in the x directions are not considered by the Nastran solution. The gust leads to a strong excitation of in-plane displacements (in the x direction), which are considered by UM/NAST and the UVL in combination with the proposed method. Higher order oscillations are part of the UM/NAST solution in that direction of deformation, but not in the solution of the proposed method. This can be explained with the fact that only the first and no higher in-plane bending modes were used in the modal basis for the proposed method.

III.E. High aspect ratio composite wingbox test case

The second test case consists of a 20-m span, generic wingbox configuration with a sweep angle of 1.8 degrees composed of quadrilateral shell elements. This three-dimensional wingbox resembles a real aircraft wing much more realistically and is built from three spars, ribs, as well as upper and lower skins. Anisotropic materials (CFRP) are used for all elements of the wing by means of Nastran *MAT2* cards. Furthermore, the thicknesses of the shell elements are reduced along the wingspan to obtain even curvature in bending deformation for typical aerodynamic loadings. No additional discrete mass elements were used for this test case. The density of all materials is $2700\,kg/m^3$, the total mass of the wingbox is $489\,kg$. The model contains 1950 nodes, 2005 elements, and 254 different anisotropic materials. It was generated using the in-house model generator *ModGen* which generates parametrized structural and aerodynamic models to be used with Nastran's structural and aeroelastic solution sequences.[17] The outer shape of the wingbox is defined by a NACA 4415 airfoil at the wing's root and a NACA4412 airfoil at the wing's tip. The model is shown in explosion view with selected details in Fig. 8.

Higher-order stiffness terms and mode components were calculated for eight modes. The ${}^pG_1^i$ and ${}^p\mathbf{\Phi}_1^i$ terms were reconstructed with the method described in Ref. 3. The reconstructed values are close to the

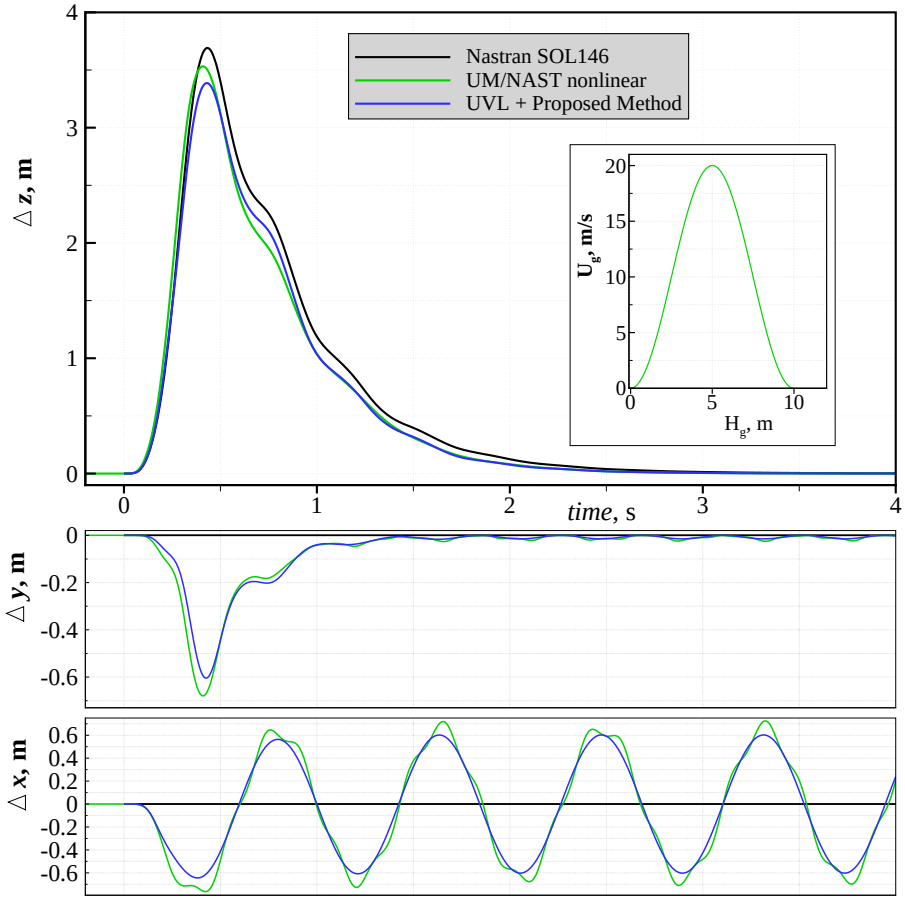

Figure 7. Comparison of *1-cos* gust encounter simulation results calculated by different methods.

corresponding natural eigenvalues of the structure but with larger differences compared to the beam test case. Table 2 lists the types and frequencies of the eight selected mode shapes of the wingbox model obtained from the finite element modal analysis and from the reconstruction method, the corresponding mode shapes are plotted in Fig. 9.

Table 2. Eigenvalues of eight selected modes of the generic wingbox model; values were obtained from a FE analysis and from a polynomial reconstruction method.

Mode	Type of mode	Eigenvalue FE analysis [Hz]	Eigenvalue reconstructed [Hz]
1	first bending	0.884	0.880
2	first bending in-plane	3.218	3.135
3	second bending	3.602	3.575
4	third bending	8.755	8.677
5	fourth bending	16.18	16.109
6	fifth bending	25.543	25.612
7	first torsion	28.302	28.386
8	sixth bending	36.171	37.411

III.F. Static simulations and validations with nonlinear Nastran results

First, a constant force in the z direction was applied at the outermost rib's nodes (at y=20m) with assumed values between 1000 N and 7000 N to simulate a static tip loading. The results are presented in Fig. 10.

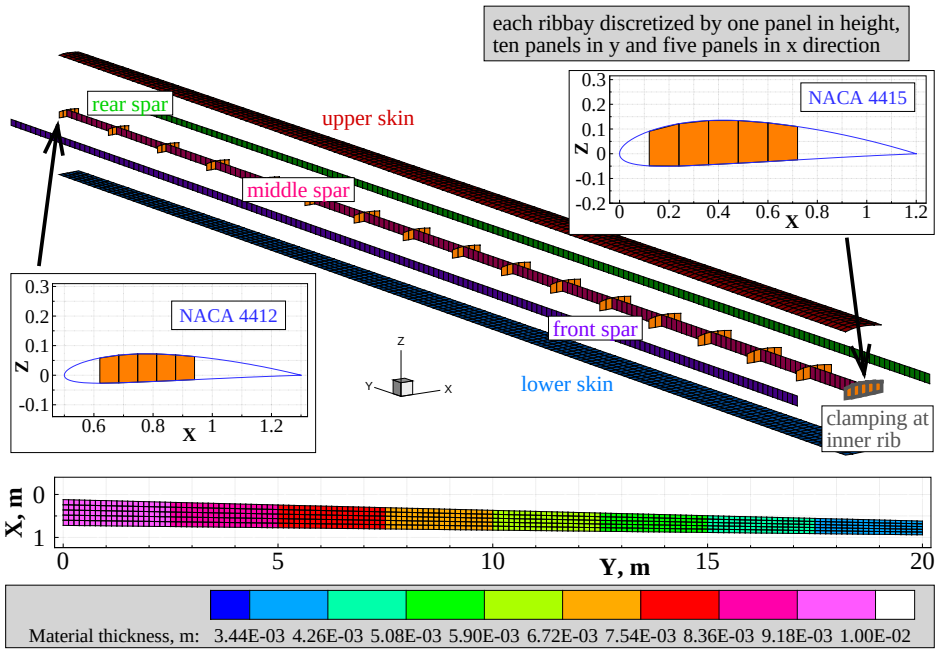

Figure 8. Layout of the wingbox made from CFRP shell elements and material thicknesses.

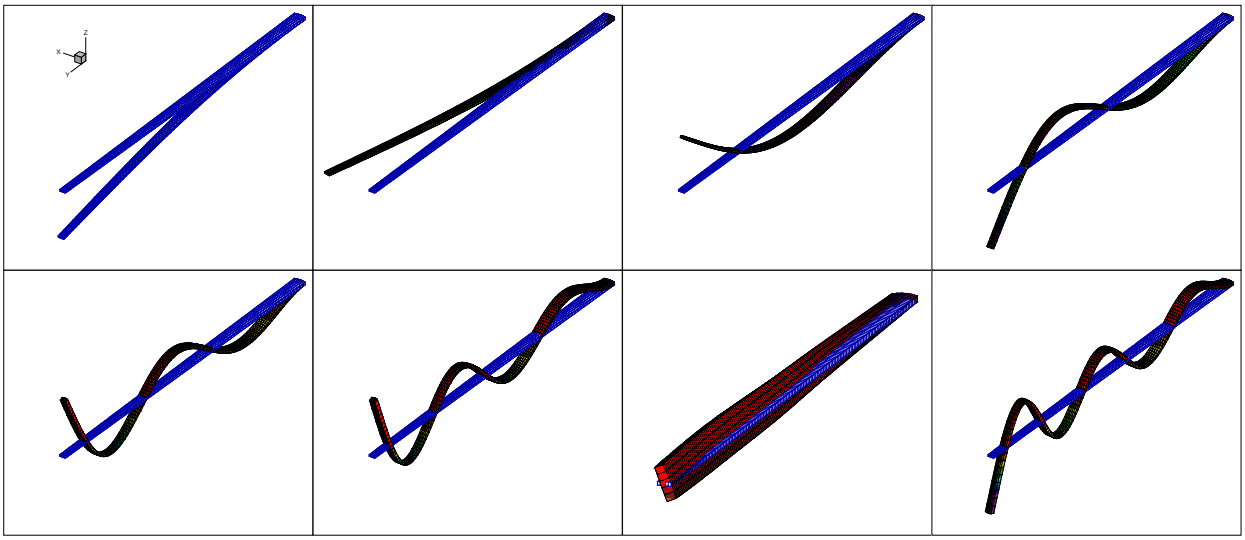

Figure 9. Selected normal mode shapes of the wing box test case (corresponding eigenvalues are given in Table 2).

Again, no follower forces and no gravity have been considered and the force is applied always onto the undeformed initial configuration of the wingbox. In this case, the values were chosen to excite deformations of the wing beyond the limit of structural linearity (up to almost 30% of the span), as can be seen in terms of the displacement in z and in y directions. As for the beam test case, the linear FE solution yields too large displacements in the z direction and completely omits the displacement in the y direction. The results of the enhanced modal approach are in fair agreement with the nonlinear reference data from Nastran also for this test case. Differences between the nonlinear Nastran solution and the proposed method become large for the last two force fields. This shows the limit of this method and demonstrates that the method should be seen as an enhancement of the linear solution, roughly in the deformation regime between 10% and 20% of the span for this test case. It must be mentioned that the upper skins of the wingbox (the skins under compression) next to the wingroot start buckling if higher loadings (in the z direction) are applied.

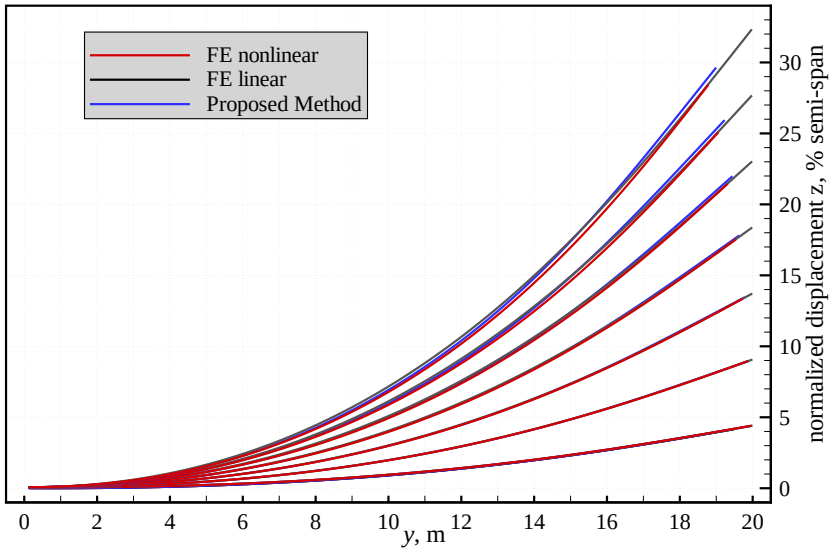

Figure 10. Comparison of the static displacement fields obtained by different methods for tip forces with values from 1000 to 7000 N applied along the z direction at the outermost rib's nodes of the wingbox.

This behaviour can be simulated by the full nonlinear Nastran solution only since no nonlinear structural solutions including buckling were used for the calculation of the higher-order stiffness and mode components.

The next test uses constant forces at each FE node in the z direction with an elliptical distribution along the wingspan. The objective is to resemble a loading which is typically obtained from aerodynamic forces. The magnitudes were again chosen to show the limits of the proposed method. The results of the simulations are presented in Fig. 11. As for the first test of the wingbox, the nonlinear reference solution from Nastran

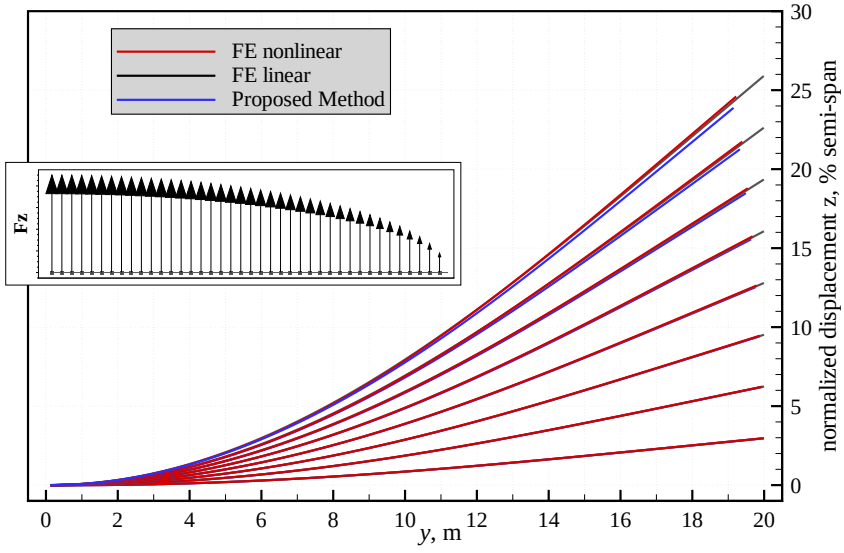

Figure 11. Comparison of the static displacement fields obtained by different methods for different elliptical force fields applied along the z direction at each node of the wingbox.

and the enhanced modal approach solution show a fair agreement regarding the displacements in the z and in y directions. The limit for the proposed method is shown to be at about 20% deformation with respect to the span of the wingbox.

A more interesting comparison is given if the elliptical force field is tilted around the local x-axis and thus has a component in y direction. The proposed method is able to consider this force field due to the quadratic mode components and the deformation and force dependent linear stiffness term, cf. Eq.(17). The result of this comparison is presented in Fig. 12, where the forces in the z direction are tilted in ± 45 degrees but the

magnitudes are kept the same. Overall displacements in the z direction are reduced for both the positive and the negative tilt angles. The linear FE solution shows large differences to the respective nonlinear results, though, because the in-plane component of the force field (in the y direction) has no effect since it acts in the local axial direction of the structure.

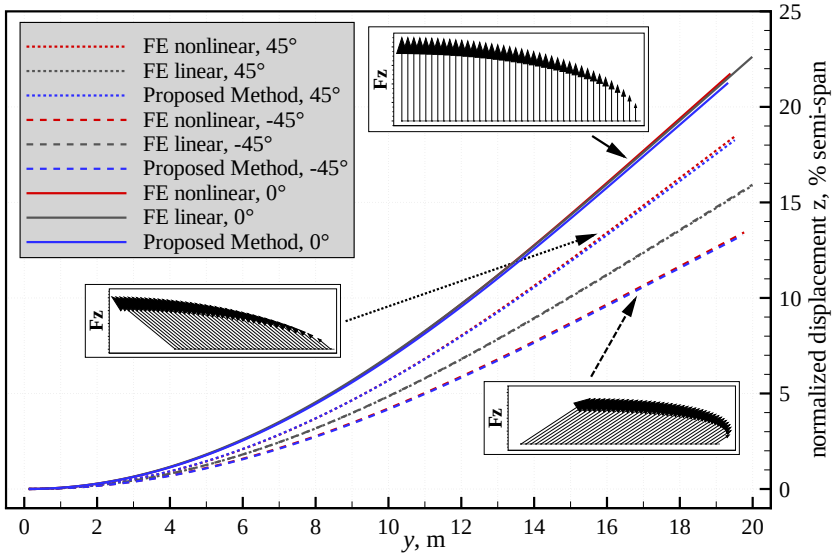

Figure 12. Comparison of the static displacement fields obtained by different methods for different elliptical force fields with components in z and y direction applied at each node of the wingbox. Forces are tilted from positive z direction by the angle given in the legend.

III.G. Static aeroelastic simulations and validation with results from MSC Nastran

Static coupling simulations were done to evaluate the potential of the method presented in terms of large deformations excited by aerodynamic forces. Here, nonlinear aerodynamic forces with respect to structural deformations are considered. In contrast to the doublet-lattice method, which is one of the most commonly used aerodynamic methods in aeroelasticity, the vortex-lattice aerodynamic model allows unlimited rotations and translations of the aerodynamic panels and calculates aerodynamic loads based on the current panel geometry. The wing is uncambered (for easier comparison with Nastran) and discretized with 64 spanwise panels and 16 chordwise panels. Its aspect ratio is 25. No specific coupling model was built for the wingbox, but all FE nodes were used to calculate a coupling matrix for force transfer and deformation interpolation.

Aeroelastic results for validation of the method were calculated using Nastran SOL144. A wing with the same geometry and equal panel discretization as the VL-grid was built for Nastran. For the transfer of forces and the interpolation of displacements, a *SPLINE1* method was used. Since Nastran uses a vortex-lattice method for static aeroelasticity and the spline definitions are similar for both methods, the results are expected to be identical in the linear regime (small deformations). The VL model and a sample aerodynamic solution in terms of the pressure coefficient difference is shown in Fig. 13.

The first aeroelastic comparison is shown in Fig. 14 in terms of the deformations as function of the root angle of attack. Both the VL solver and the Nastran solution (SOL144) are based on incompressible aerodynamics (the Mach number in Nastran is therefore set to zero in the corresponding aerodynamic card). The dynamic pressure is 3750 Pa. Both the Nastran and the VL solution in combination with a linear structural solution yield comparable results —if not exactly the same —for all angles of attack applied. The difference is most likely to come from the solution process. The VL aeroelastic solution is a static coupling process in which aerodynamic forces and structural deformations are converged iteratively. However, two effects are involved that act against each other. First, the increase in the panel area due to the linear structural solution, shown in Fig. 15, and second, the tilting of the aerodynamic lifting forces which results in a component in the y direction. The deformations of the nonlinear solution, which was obtained by static coupling of the VL solver with Nastran's SOL400 sequence, and the deformations of the proposed method show good agreement. Differences become significant starting at tip deflections of about 25%.

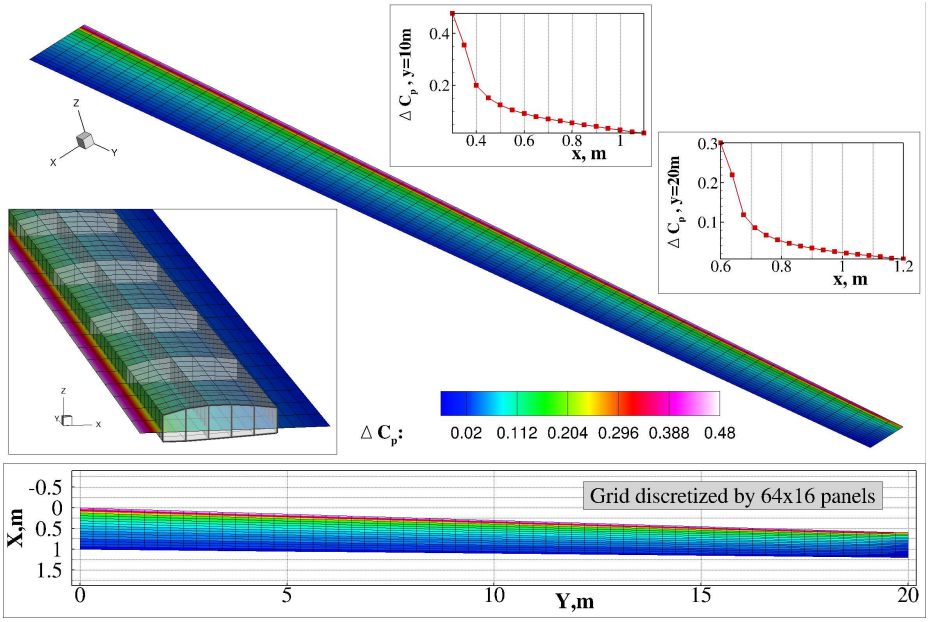

Figure 13. Vortex Lattice aerodynamic model of the wingbox with ΔC_p distribution (incompressible solution, dynamic pressure=3750Pa, AoA=1deg).

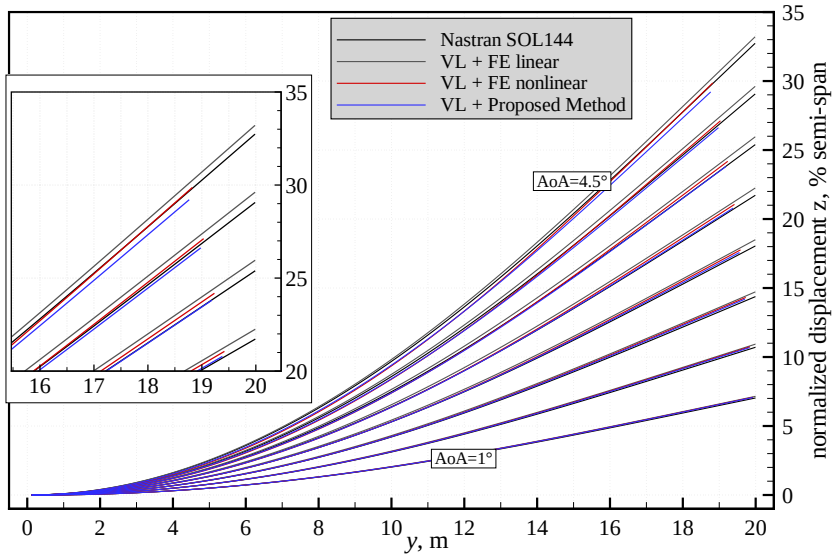

Figure 14. Comparison of static coupling results calculated by different methods.

Structural loads will be discussed in addition to deformations to evaluate the proposed method from a sizing point of view. This will answer the question of how deformations influence structural loads. Therefore, the forces and moments at the wing root with components in x, y, and z directions are compared as function of the angle of attack at the wing root in Fig. 16. Large differences between the two linear and the two nonlinear solutions are obtained for the shear force F_z at the wing root. The proposed method is in good agreement with the nonlinear reference solution, although it yields slightly higher loads (which can be taken as conservative). The Nastran SOL144 results show no forces in x and y directions due to the calculation of the aerodynamic forces. The VL solution calculates the induced drag, though. The loads F_x agree between the three VL solutions, but the forces from the VL and linear FE solution in the y direction show large difference. This can be explained with the increase in the surface area, as shown in Fig. 15. As expected, good agreement is given between the moments at the wing root around the y and z axes. It must be mentioned that F_x is negative and thus M_z is positive due to the fact that in the body fixed system, the lift

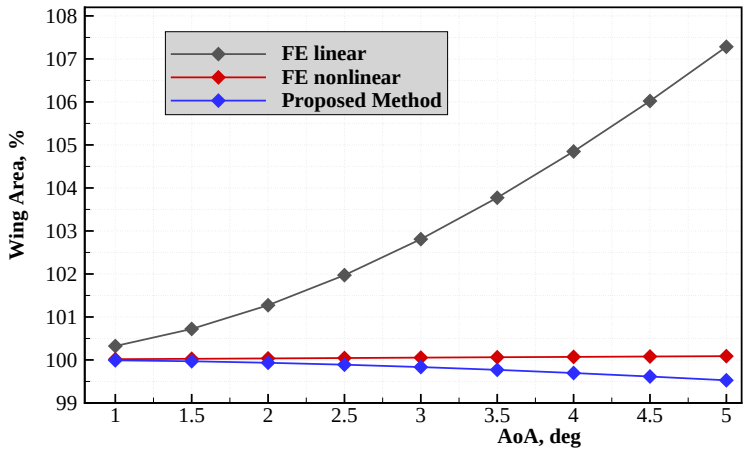

Figure 15. Changes in the wing's entire surface area due to deformation.

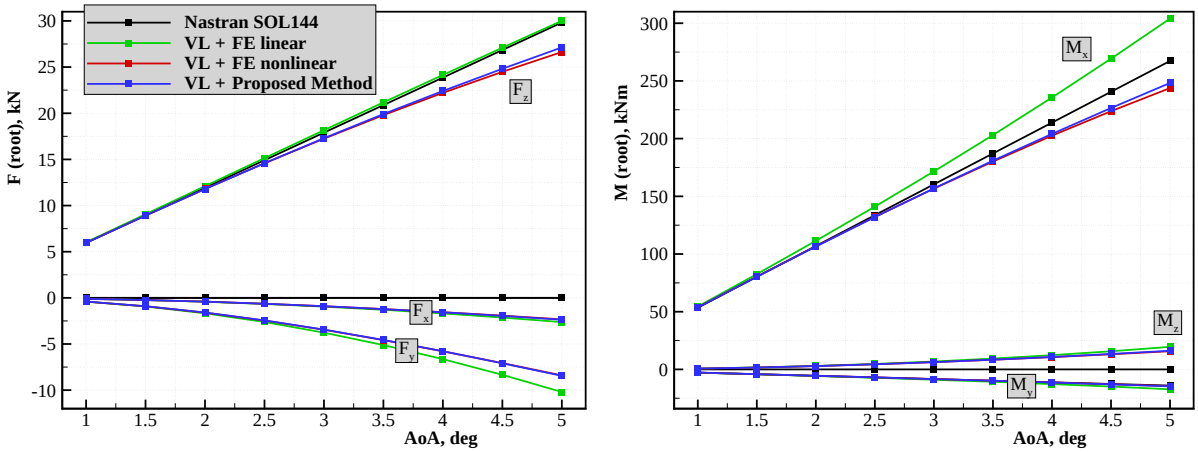

Figure 16. Summed forces in x, y, and z directions, moments at x, y, and z axes at the wing root as function of angle of attack.

force has a (positive) component in x direction. The moment around the y axis is negative due to the slight sweep back of the wing. Most important is the comparison of the wing root bending moment M_x. Here, the VL and linear structural solution yields a much higher bending moment compared to the nonlinear and even to the Nastran solution. The tilting of the aerodynamic force vectors, as is considered by the VL solution, keeps them perpendicular to the wing's panels and thus leads to higher bending moments along the wing span and at the root. However, the increase in panel area additionally increases this bending moment. The aerodynamic forces from the Nastran solution only have a component in the z direction, thus lowering the bending moment M_x even if the panel area is increased. The bending moment from the nonlinear Nastran solution and the proposed method are in fair agreement, again the enhanced modal approach yields larger values. The most important conclusion from the loads point of view is that an aerodynamically nonlinear solution in terms of displacements (such as the one obtained from the VL method) should not be used in combination with a linear structural solution. This overestimates the bending moment M_x as discussed above.

III.H. Dynamic aeroelastic simulations and validation with results from MSC Nastran

Results and validations of different dynamic solution methods are presented in the following for the same model. Unsteadiness is introduced by means of unsteady boundary conditions, in this case by a vertical disturbance velocity that superimposes the steady uniform flow field.

The first unsteady test case consists of a 1-cos type gust encounter. The wing is initially at rest, i.e., no steady state deformation is used as initial condition. This is realized in the unsteady VL solution by simply

setting the angle of attack to zero degree (the wing's airfoil is uncambered). The uniform flow velocity is set to $50\,m/s$, the gust disturbance velocity is $14\,m/s$, and the gust gradient $14\,m$. It must be mentioned that no stall effects are modeled in the UVL solver. The maximum of the time dependent angle of attack during the gust encounter reaches comparatively high values due to the high gust velocities (which were chosen to excite large deformations). This would eventually lead to flow separation from an aerodynamic point of view, but this effect is neglected here. The results of three different methods (Nastran SOL146, UVL and FE linear, and UVL and proposed method) are compared in terms of the time dependent displacements of four selected structural nodes. These nodes are located at y=$5\,m$, $10\,m$, $15\,m$, and $20\,m$ on the upper surface of the wing, as shown in Fig. 17. Unfortunately, no fully nonlinear results are available for this comparison. It

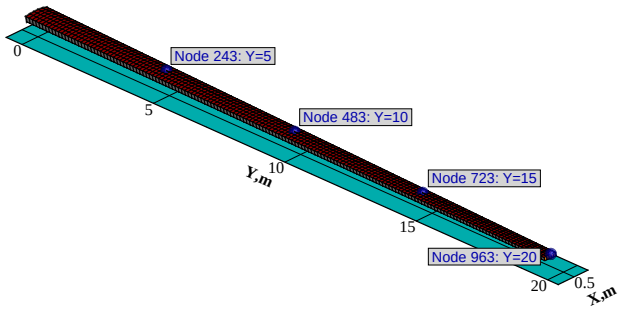

Figure 17. Points on the wing's upper surface for which time dependent displacements will be presented.

is intended to couple the UVL solver to Nastran SOL400 in the future. Results of the first unsteady test case are presented in Fig. 18. As can be seen, the Nastran and the linear UVL with the linear structural solution are in good agreement with slightly higher deformations in the z direction for the UVL results, similar as for the static coupling results. The motion of the wing is governed by low frequency structural modes in these results. The proposed method yields lower deformations in the z direction and shows displacements in the y

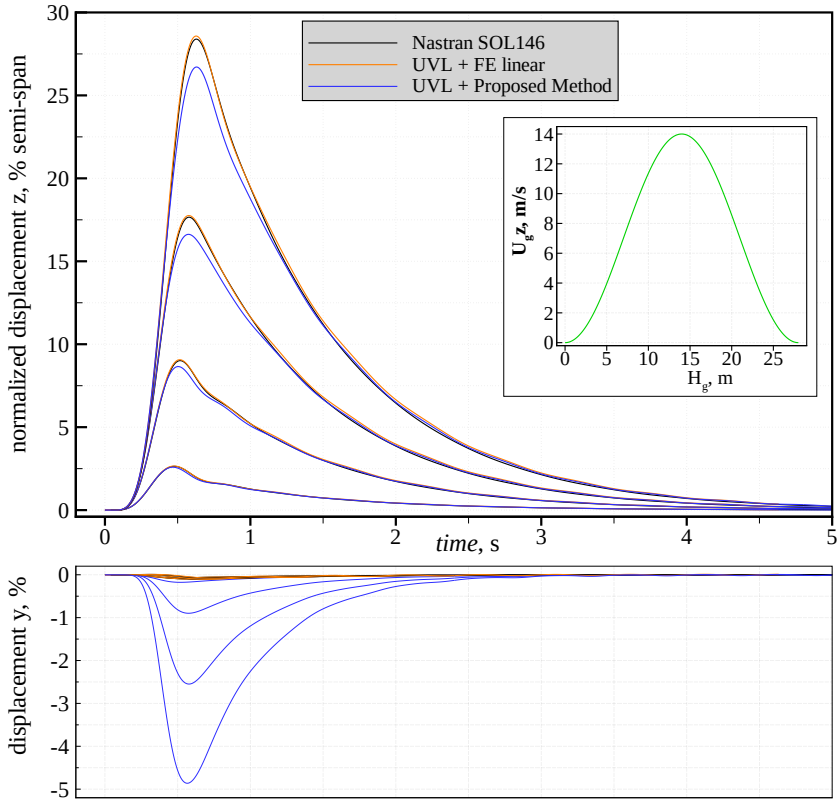

Figure 18. Displacements of four structural nodes as function of time of *1-cos* type gust encounter. Results from gust with disturbance velocity of $14\,m/s$, and gust gradient of $14\,m$.

direction, as expected. Deformations of this test case reach about 28% for the linear solutions, the proposed method reaches about 26% with respect to the span of the wing. The time dependent motion of the nodes is generally in good agreement among the three results, besides the differences in the displacements due to the different kinematical relationships.

The second unsteady test case uses the same vertical gust velocity as before, but the gust gradient is reduced to $9\,m$. The goal is to excite higher frequency components in the solution. The results are given in Fig. 19. Nodal deformations are lower for this test case as expected, the maximum tip deflection is

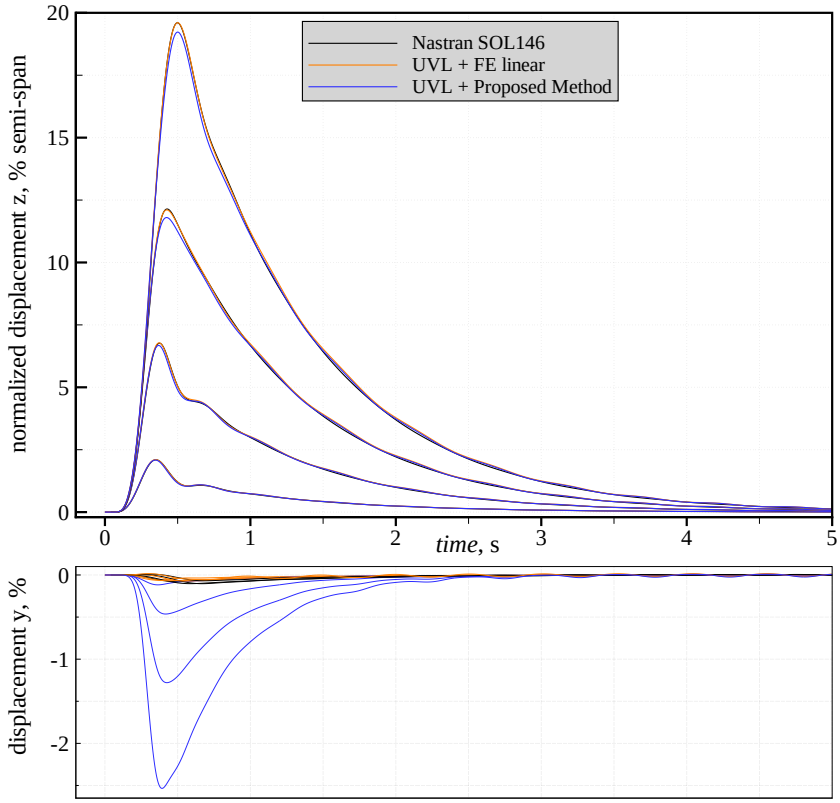

Figure 19. Displacements of four structural nodes as function of time of *1-cos* type gust encounter. Results from gust with disturbance velocity of $14\,m/s$, and gust gradient of $9\,m$.

about 19% of span. The difference between the linear solutions is very small, and the proposed method yields slightly less displacements in the z direction but accounts for the foreshortening effect. A closer look at the time dependent generalized coordinates gives insight into the contribution of the individual modes to the unsteady deformation of the structure. Fig. 20 shows that the first bending mode has the largest contribution, followed by the second and the third bending modes. It is interesting to mention that the UVL solver considers induced drag and thus excites the first in-plane bending mode (mode two in Fig. 20) as the gust passes the wing which is only barely damped.

Another test case to demonstrate the power of the enhanced modal approach is given by the simulation of a lateral gust, i.e., the gust disturbance velocity is in the positive or negative y direction. This test case is comparable to the steady structural test case in which the force field originally along the z direction has been tilted to get components in the y direction, cf. Fig. 12. The gust of the next test case is again of 1-cos shape, its velocity is $14\,m/s$ in the positive y direction, and the gust gradient is $9\,m$. Unfortunately, no reference solution from Nastran is available for this test case, since the wing has no dihedral in the unloaded state and a steady trim solution is not considered in the unsteady solution sequence. The VL solution starts from an initial trim solution which was generated by setting the angle of attack to a certain value. This trim solution serves as initial condition for the unsteady solutions (linear and nonlinear), and because the wing now has a surface projection in the y direction, the lateral gust acts on the displaced panels and excites aerodynamic forces, mainly in the y direction. Fig. 20 shows the results of the UVL solver coupled with the linear and the enhanced modal approach solutions. It can be seen that both solutions correctly simulate an unsteady

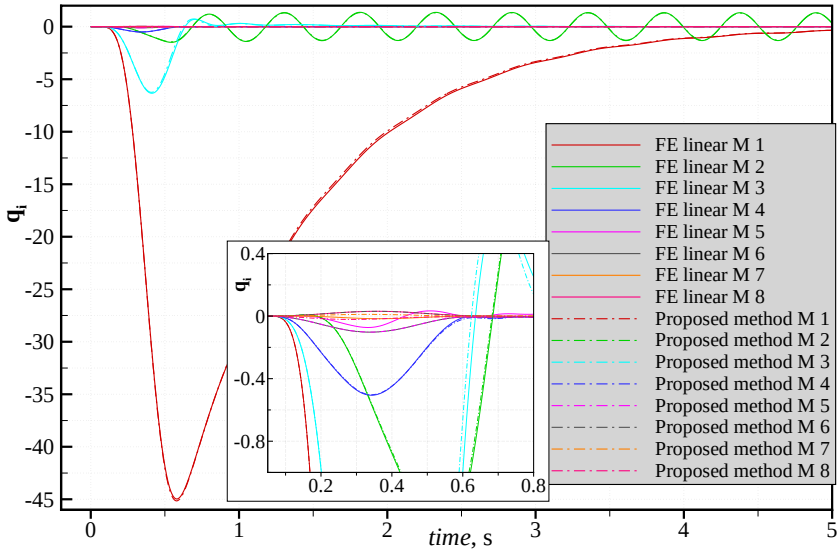

Figure 20. Modal participation factors (generalized coordinates) as function of time for the second unsteady test case.

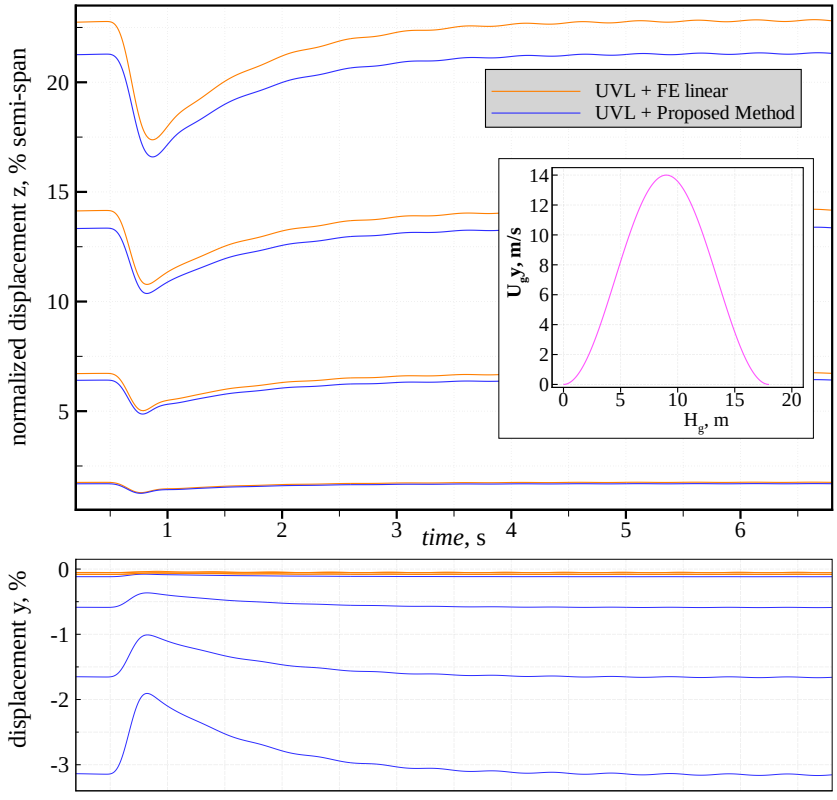

Figure 21. Displacements of four structural nodes as function of time of a lateral *1-cos* type gust encounter. Results from gust with disturbance velocity of $14\,m/s$ in the positive y direction, and gust gradient of $9\,m$.

displacement in the z direction which reduces the initial trim displacements. The proposed method yields lower displacements in the z direction and considers displacements in the y direction.

The next test case uses the same initial conditions and setup, but the lateral gust directs in the negative y direction. The results are presented in Fig. 20. Here, the deformations are increased because the additional gust load leads to higher lifting forces on the wing. Again, the displacements in the y direction are captured by the enhanced modal approach only.

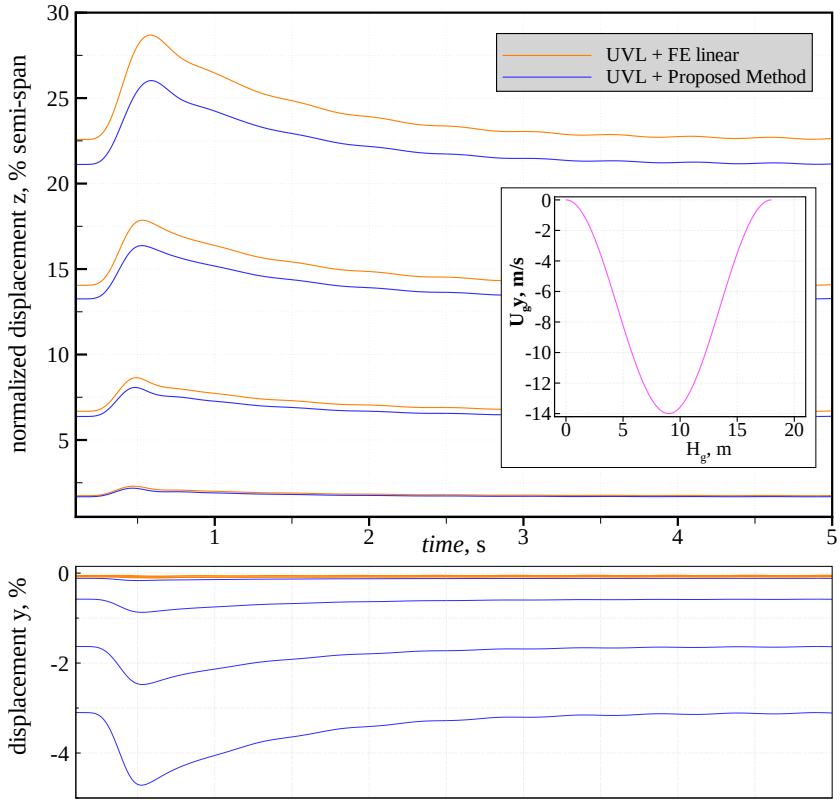

Figure 22. Displacements of four structural nodes as function of time of a lateral *1-cos* type gust encounter. Results from gust with disturbance velocity of $14\,m/s$ in the negative y direction, and gust gradient of $9\,m$.

IV. Conclusion and Outlook

A method was presented that enhances the classical modal approach used in structural dynamics and aeroelastic applications towards large geometric deformations. Nonlinearities in the force-displacement relationships and in the geometrically nonlinear deformation field are accounted for. Therefore, the classical modal approach governing equations are enhanced with terms of higher order for the stiffness and the reconstruction of the displacement field in physical coordinates from modal space. Based on these terms, nonlinear static and dynamic governing equations were obtained in which the generalized stiffnesses are depending on the forces applied to the structure. It was shown that the quadratic component of the higher order modes are needed to account for in-plane loadings, which are present in typical aerodynamic forces when lifting panels undergo large rotations. In this work, the method was successfully applied to a beam type model and a more complex wingbox made from composite shell elements. Static and dynamic results showed that the proposed method can acceptably reflect the geometrically nonlinear deformation field at large bending deformations up to values of approximately 25% of the wing's semi-span. However, it must be mentioned that the linear FEM yields good results in terms of deformations up to about 10% tip displacement for the test cases presented. Static and dynamic aeroelastic simulations show that the proposed method surpasses the linear modal approach by considering lateral forces in the solution which arise from rotated lifting panels. From the structural loads point of view, it was shown that a geometrically nonlinear aerodynamic method (such as the VL method) should not be used in combination with a linear structural solution in the regime of large deformations, since bending moments will be noticeably overestimated. In this case, a linear aerodynamic method in combination with a linear structural solution (Nastran SOL144) yields better results when compared to the nonlinear reference solution. The next step for the improvement and validation of the method proposed will be the static and dynamic modeling of the complex jet transport aircraft wingbox shown in Fig. 1.

V. Acknowledgments

Parts of this work were carried out during two internships of the first author at the Active Aeroelasticity and Structures Research Lab at the University of Michigan. The authors would like to thank the entire team of the laboratory for their support. Furthermore, the support of Johannes Dillinger from the DLR Institute of Aeroelasticity for the generation of the wingbox model is gratefully acknowledged.

References

[1]Cesnik, C. E. S., Palacios, R., and Reichenbach, E. Y., "Reexamined Structural Design Procedures for Very Flexible Aircraft," *Journal of Aircraft*, Vol. 51, No. 5, 2014, pp. 1580–1591.

[2]Su, W. and Cesnik, C. E. S., "Strain-Based Analysis for Geometrically Nonlinear Beams: A Modal Approach," 53^{rd} AIAA/ASME/ASCE/AHS/ASC Structures, Structural Dynamics and Materials Conference, Honolulu, Hawaii, April 2013.

[3]Ritter, M., Cesnik, C. E., and Krüger, W. R., *An Enhanced Modal Approach for Large Deformation Modeling of Wing-Like Structures*, AIAA SciTech, 56^{th} AIAA/ASME/ASCE/AHS/ASC Structures, Structural Dynamics, and Materials Conference, Kissimmee, Florida, Jan 2015.

[4]Mignolet, M. P., Przekop, A., Rizzi, S. A., and Spottswood, S. M., "A review of indirect/non-intrusive reduced order modeling of nonlinear geometric structures," *Journal of Sound and Vibration*, Vol. 332, No. 10, 2013, pp. 2437 – 2460.

[5]Kim, K., Radu, A. G., Wang, X. Q., and Mignolet, M. P., "Nonlinear reduced order modeling of isotropic and functionally graded plates," *International Journal of Non-Linear Mechanics*, Vol. 49, No. 0, 2013, pp. 100 – 110.

[6]Wang, X. Q., Perez, R. A., and Mignolet, M. P., "Nonlinear Reduced Order Modeling of Complex Wing Models," 54^{th} AIAA/ASME/ASCE/AHS/ASC Structures, Structural Dynamics, and Materials Conference, Boston, Massachusetts, Apr 2013.

[7]Kuether, R. J. and Allen, M. S., "Nonlinear Modal Substructuring of Systems with Geometric Nonlinearities," Structures, Structural Dynamics, and Materials and Co-located Conferences, 54^{th} AIAA/ASME/ASCE/AHS/ASC Structures, Structural Dynamics, and Materials Conference, Boston, Massachusetts, Apr 2013.

[8]Kuether, R. J. and Allen, M. S., "Substructuring with Nonlinear Reduced Order Models and Interface Reduction with Characteristic Constraint Modes," AIAA SciTech, 55^{th} AIAA/ASME/ASCE/AHS/ASC Structures, Structural Dynamics, and Materials Conference, National Harbor, Maryland, Jan 2014.

[9]Segalman, D. J. and Dohrmann, C. R., "Dynamics of Rotating flexible Structures by a Method of Quadratic Modes," Sandia National Laboratories, Structural Dynamics Division, Albuquerque, New Mexico, 1990.

[10]Segalman, D. J. and Dohrmann, C. R., "A Method for Calculating the Dynamics of Rotating Flexible Structures, Part1: Derivation," *ASME Journal of Vibration and Acoustics*, Vol. 118, 1996, pp. 313–317.

[11]van Zyl, L. H., Sutherland, A. N., and Rossouw, P. S., "Parabolic Mode Shapes: What they are, where to get them and what to do with them," International Forum on Aeroelasticity and Structural Dynamics, Seattle, Washington, 2009.

[12]van Zyl, L. H. and Mathews, E. H., "Quadratic Mode Shape Components From Linear Finite Element Analysis," *ASME Journal of Vibration and Acoustics*, Vol. 134, Feb. 2012.

[13]Shames, I. H. and Dym, C. L., *Energy and Finite Element Methods in Structural Mechanics*, Hemisphere Publishing Corporation, 1985.

[14]Su, W. and Cesnik, C. E. S., "Nonlinear Aeroelasticity of a Very Flexible Blended-Wing-Body Aircraft," *Journal of Aircraft*, Vol. 47, No. 5, Sep 2010, pp. 1539–1553.

[15]Anon., *MSC Nastran 2012 Quick Reference Guide*, MacNeal-Schwendler Corporation, 2011.

[16]Katz, J. and Plotkin, A., *Low-Speed Aerodynamics*, Cambridge Aerospace Series, Cambridge University Press, 2001.

[17]Klimmek, T., "Parameterization of topology and geometry for the multidisciplinary optimization of wing structures," Proceedings CEAS 2009, CEAS 2009 - European Air and Space Conference, Manchester, United Kingdom, Oct 2009.